Biosensors and Bioelectronics 140 (2019) 111355

Contents lists available at ScienceDirect

Biosensors and Bioelectronics

journal homepage: www.elsevier.com/locate/bios

Self-sacrificial label assisted electroactivity conversion of sensing interface for ultrasensitive electrochemical immunosensor

Shuang Yin, Zhanfang Ma*

Department of Chemistry, Capital Normal University, Beijing, 100048, China

ARTICLE INFO

Keywords:
Self-sacrificial label
Fe^{3+}-loaded polydopamine nanoparticles
Electroactivity conversion
Sensitivity amplification
Tumor marker

ABSTRACT

Sensitivity amplification strategies in electrochemical immunoassays are mainly limited by redox signal leaking, degradation of catalytic activity caused by layers of decoration and the large hindrance effect caused by immunoprobes. Herein, we developed an innovative sensitivity amplification strategy based on the self-sacrificial label-assisted electroactivity conversion of a sensing interface, utilizing Fe^{3+}-loaded polydopamine (Fe^{3+}-PDA) nanoparticles as the self-sacrificial labels, which can be decomposed under acidic conditions and release Fe^{3+}. When the assembled sensing interface was immersed in a prussian blue (PB) precursor solution (a mixed solution of 0.1 M KCl, 0.1M HCl and 1 mM $K_3Fe(CN)_6$), the as-formed sandwich-type structure was destroyed due to the decomposition of Fe^{3+}-PDA caused by HCl in PB precursor solution, resulting in the reduce of interface resistance. The released Fe^{3+} reacted with the PB precursor solution and triggered the growth of electroactive PB nanoparticles (PB NPs) on the sensing interface. Assisted by self-sacrificial Fe^{3+}-PDA, the sensing interface was converted from electrochemically inactive to electroactive with a strong redox signal, high catalytic activity, and decreased interface resistance. The PB NPs can catalyse H_2O_2 to amplify the redox signal, thus improving sensitivity. The redox signal and catalysts were generated in the final assembly step, which can avoid signal leaking and decreases of catalytic activity caused by layers of decoration. The decomposition of Fe^{3+}-PDA can eliminate the large hindrance effect of the immunoprobe. Ultrasensitive quantification of carbohydrate antigen 125 (CA 125) was realized with a detection range from 0.00001 to 1000 U mL^{-1} and detection limit of 0.25×10^{-6} U mL^{-1}.

1. Introduction

Sensitive and accurate assays of tumor markers are effective ways to diagnose cancer in the early stages (Atkinson et al., 2001; Sawyers, 2008). A variety of analytical methods, such as colorimetric (Hua et al., 2016; Tang et al., 2012), photoelectrochemical (Cai et al., 2018; Han et al., 2017), electrochemiluminescent (Han et al., 2011; Zhou et al., 2015) and electrochemical assays (Tang et al., 2017; Zhao et al., 2019) have been put forward to enable the sensitive detection of tumor markers. In comparison with other approaches, electrochemical assays are considered the most prospective technique due to their high sensitivity, low-cost, simplicity, and fast response (Luo and Davis, 2013; Wilson, 2005). To meet the increasing demands of clinical diagnosis, various effective sensitivity amplification strategies have been developed.

Sensitivity amplification via the enrichment of electroactive species has shown to be an effective approach. This strategy involves some types of nanocarriers to gather electroactive species, such as mesoporous silica (Tang et al., 2010; Zhang et al., 2018), porous carbon (Xu et al., 2015; Yang et al., 2015a), hydrogels (Yin et al., 2017; Zhao et al., 2018), polymers (Wang et al., 2015), and hollow metal nanoparticle (Wang et al., 2014). Substrates or immunoprobes with strong electrochemical signals can be obtained through enrichment of electroactive species. In an electrochemical immunoassay, catalytic amplification has attracted special attention due to the prominent improvement of sensitivity. Bio-enzymes or nanocatalysts with high catalytic efficiency are commonly employed to facilitate interfacial electron transfer (Shen et al., 2015; Wang et al., 2016) and produce electroactive substance (Yang et al., 2015b; Zhang et al., 2016) and precipitation (Hou et al., 2014; Zheng and Ma, 2018), leading to sensitive analytical performance. Although these strategies enhance the sensitivity of electrochemical assays, the following challenges still exist: (1) the electroactive substrates or immunoprobes may suffer from the problem of signal leaking; (2) the catalytic activity of bio-enzymes or nanocatalysts decreases noticeably after layers of decoration (Li et al., 2018); and (3) the large hindrance effect of immunoprobes is adverse to

* Corresponding author.
E-mail address: mazhanfang@cnu.edu.cn (Z. Ma).

https://doi.org/10.1016/j.bios.2019.111355
Received 19 March 2019; Received in revised form 23 May 2019; Accepted 26 May 2019
Available online 30 May 2019
0956-5663/

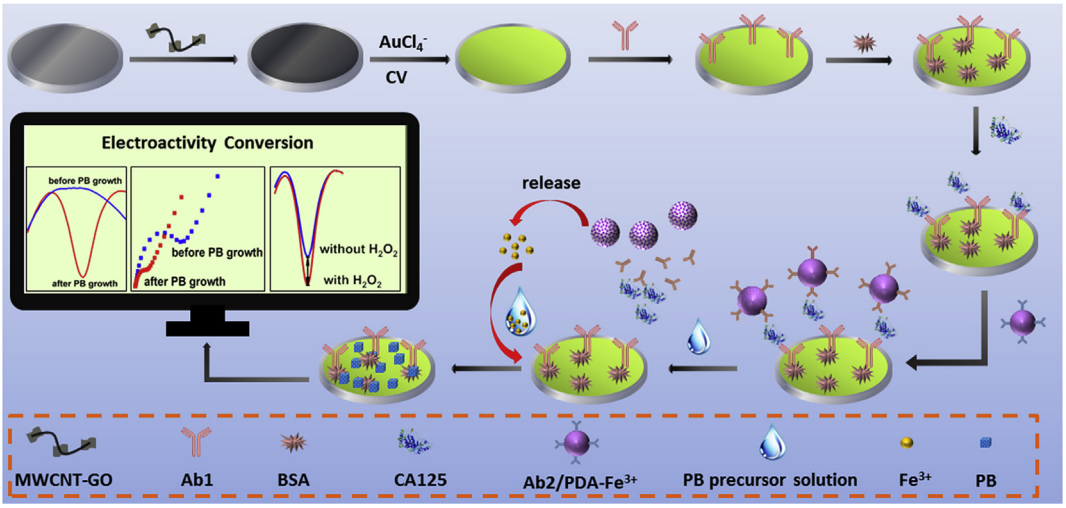

Scheme 1. Schematic Diagram of self-sacrificial label assisted electroactivity conversion of sensing interface for ultrasensitive detection of CA 125.

interfacial electron transfer, leading to severe degradation of the signal response (Chen et al., 2006; Wei et al., 2017).

In this study, an innovative sensitivity amplification strategy based on self-sacrificial label-assisted electroactivity conversion of a sensing interface was developed (Scheme 1). Fe^{3+}-loaded polydopamine (Fe^{3+}-PDA) nanoparticles, served as self-sacrificial labels, can be decomposed under acidic conditions and release Fe^{3+}. The electroactivity conversion encouraged sensitivity amplification was achieved in two steps. First, when dipped in acidic prussian blue (PB) precursor solution (a mixed solution of 0.1 M KCl, 0.1 M HCl and 1 mM $K_3Fe(CN)_6$), the as-formed sandwich-type structure was destroyed due to the decomposition of Fe^{3+}-PDA caused by HCl in PB precursor solution, leading to the decrease of interface impedance. Second, the released Fe^{3+} triggered the growth of PB nanoparticles (PB NPs) on the sensing interface, after which the sensing interface exhibited a strong redox signal and high catalytic activity towards H_2O_2. In addition, multiwalled carbon nanotube-graphene oxide (MWCNT-GO) complexes provided a favorable platform for the generation of abundant PB NPs and benefited the conductivity of the sensing interface. Carbohydrate antigen 125 (CA 125) was assayed to validate the feasibility of this sensitivity amplification strategy. Assisted by the self-sacrificial Fe^{3+}-PDA NPs, the electrochemical sensing interface converted from being electrochemically inactive to electroactive with a strong redox signal, high catalytic activity and decreased interface resistance, resulting in the ultrasensitive determination of CA 125.

2. Experimental

2.1. Reagents and materials

Graphene oxide (GO) was purchased from Nanjing JCNANO Tech Co. Ltd (Nanjing, China). Multi-walled carbon nanotube (MWCNT) was obtained from Shanghai Aladdin Bio-Chem Technology Co., Ltd. Iron (III) chlordehexahydrate ($FeCl_3$) was obtained from Sinopharm Chemical Reagent Co., Ltd (Shanghai, China). Sodium hydroxide (NaOH), potassium ferrocyanide, potassium ferricyanide, potassium chloride (KCl), sodium dihydrogen phosphate dehydrate (NaH_2PO_4 $2H_2O$) and disodium hydrogen phosphate dodecahydrate (Na_2HPO_4 $12H_2O$) were achieved from Beijing Chemical Reagents Company (Beijing, China). Ascorbic acid (AA), dopamine hydrochloride (DA), uric acid (UA) and hydrogen peroxide (H_2O_2) were bought form Alfa Aesar (Tianjin, China). Carbohydrate antigen 125 (CA 125, from human pleural fluids, calibrator grade), coated anti-CA 125 (Ab_1), labeled anti-CA 125 (Ab_2), cytokeratin 19 antigen (CK19), carbohydrate antigen 153 (CA 153), neuron specific enolase (NSE), and squamous Cell Carcinoma Antigen (SCCA) obtained from Shanghai Linc-Bio Science Company (Shanghai, China). Human immunoglobulin G (IgG) and bovine serum protein (BSA) was purchased from Beijing Xinjinke Bioechnology Co. Ltd (Beijing, China). Clinical human serum samples were provided by Deyi Diagnostics (Beijing, China). All solutions were prepared using ultrapure water (resistivity greater than 18 MΩ cm).

2.2. Apparatus

Transmission electron micrographs were determined on a JEOL-100CX transmission electron microscope (TEM). Scanning electron micrographs and energy disperse spectroscopy (EDS) were obtained with a HITACHI S-4800 SEM (HITACHI, Japan). Fourier transforminfrared (FTIR) spectra were performed on a VECTORTM 22 spectrometer (Bruker). Zeta potential measurements were conducted with Zetasizer Nano ZS (Malvern Instruments Co., UK). UV–vis measurements were carried out on a UV-2550 UV–Vis spectrophotometer (Shimadzu, Japan). All electrochemical experiments were achieved through a CHI-660 electrochemical workstation (Chenhua Instruments Co., Shanghai, China). Ultrapure water used in the experiment was purified through Olst ultrapure K8 apparatus (Olst, Ltd., resistivity > 18.25 MΩ cm). A three-electrode system was used including a glassy carbon electrode (GCE, 4 mm in diameter) as the working electrode, Ag/AgCl electrode (saturated KCl) as the reference electrode, and a platinum wire as counter electrode.

Details about the preparation of multiwalled carbon nanotube-graphene oxide complexes (MWCNT-GO), Fe^{3+}-loaded polydopamine (Fe^{3+}-PDA) nanoparticles and immunoprobes are given in the Supplementary Material.

2.3. Construction of the sensing platform

The GCE was polished with 0.05 μm alumina slurry and washed with water by ultrasonic cleaning three times. Next, 6 μL MWCNT-GO dispersions were coated on the GCE. After drying, CV was performed scanning from −1.0 V to 0.20 V at a rate of 50 mV s^{-1} for 6 cycles in 5 mM $HAuCl_4$. Subsequently, 80 μL Ab_1 (200 μg mL^{-1}) was incubated on Au/MWCNT-GO/GCE for 12 h at 4 °C. To block the nonspecific binding sites, Ab_1/Au/MWCNT-GO/GCE was then treated with 20 μL BSA (1%, w/w) at 37 °C for 1 h.

2.4. Measurement procedure

CA 125 standard solutions with different concentrations were incubated on BSA/Ab_1/Au/MWCNT-GO/GCE at 37 °C for 1 h. Then, 20 μL

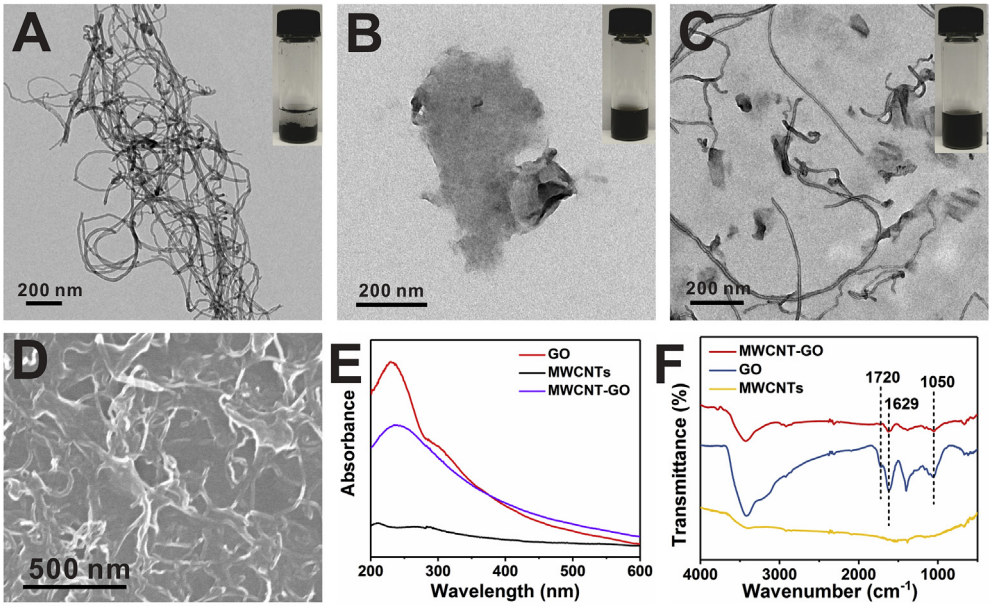

Fig. 1. TEM micrographs of MWCNTs (A), GO (B), MWCNT-GO (C). SEM micrographs of MWCNT-GO (D). UV–vis spectra (E) and FTIR spectra (F).

immunoprobes were covered on CA 125/BSA/Ab_1/Au/MWCNT-GO/GCE at 37 °C for 45 min. After that, 40 μL prussian blue (PB) precursor solution (a mixed solution of 0.1 M KCl, 0.1M HCl and 1 mM $K_3Fe(CN)_6$) was incubated on electrode surface at 25 °C for 40 min. The detection process was conducted by square wave voltammetry (SWV) in PBS (pH 7.4) containing 0.1 mM H_2O_2.

3. Results and discussion

3.1. Characterization of MWCNT-GO

The prepared MWCNTs, GO and MWCNT-GO were characterized by TEM. The pristine MWCNTs could not be dispersed evenly in water (inset in Fig. 1A) and tended to aggregate due to the hydrophobicity (Fig. 1A). In contrast, GO was well-dispersed in water (inset in Fig. 1B) due to the abundant oxygen-containing groups and displayed a 2D flake-like structure (Fig. 1B). Interestingly, a stable dispersion of MWCNT-GO complexes was formed (inset in Fig. 1C), and MWCNTs were randomly adsorbed on the GO sheets (Fig. 1C). The hydrophilic oxygen groups of GO maintain the water solubility of the MWCNT-GO complexes (Chao et al., 2010). The MWCNT-GO was also characterized by SEM, as displayed in Fig. 1D. A large amount of MWCNTs were observed on GO sheets, indicating the formation of MWCNT-GO complexes. MWCNTs, GO and MWCNT-GO were also analyzed by UV–vis spectroscopy (Fig. 1E). The absorption peak at 230 cm^{-1} was assigned to the π-π transitions of aromatic C–C bonds of GO (Chao et al., 2010). FTIR spectra were obtained to confirm the formation of MWCNT-GO (Fig. 1F). The absorption bands at 1629 and 1720 cm^{-1} arose from carbonyl stretching vibration, and the band at 1050 cm^{-1} was derived from the vibration of C–O (epoxy or alkoxy) or C–OH (carboxyl or phenol) (Guo et al., 2009). These peaks can be observed in the spectra of MWCNT-GO and GO, indicating the formation of MWCNT-GO.

3.2. Characterization of Fe^{3+}-PDA nanoparticles

The morphologies of PDA and Fe^{3+}-PDA nanoparticles were characterized by TEM. PDA nanoparticles displayed spherical structure with diameters around 200 nm (Fig. 2A), and no significant difference in morphology was observed between Fe^{3+}-PDA and PDA (Fig. 2B). EDS was conducted to investigate the detailed compositions of PDA and Fe^{3+}-PDA nanoparticles, in which obvious peaks for C, N, and O were

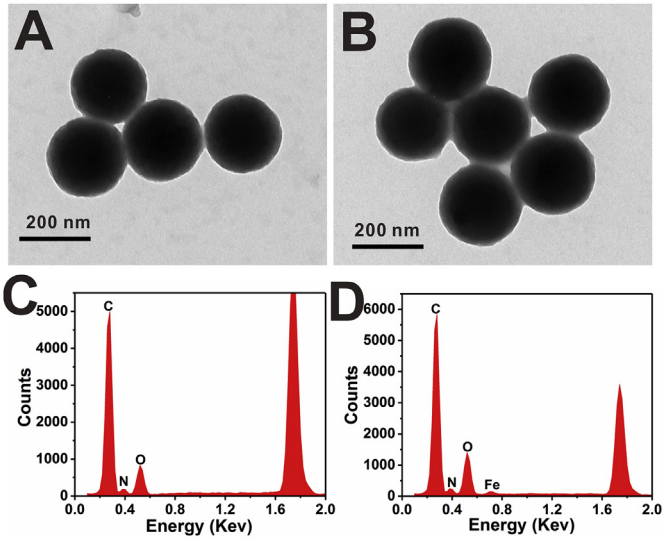

Fig. 2. TEM micrographs of PDA (A), Fe^{3+}-PDA (B). EDS spectra of PDA (C), Fe^{3+}-PDA (D).

obtained from PDA particles (Fig. 2C). After loading Fe^{3+} ions, a clear Fe peak was observed in the Fe^{3+}-PDA NP spectrum, suggesting the successful synthesis of Fe^{3+}-PDA.

3.3. Characterization of the immunosensor

To monitor the stepwise construction of the immunosensor, cyclic voltammetry (CV) was implemented in 5 mM $[Fe(CN)_6]^{3-/4-}$ solution containing 0.1 M KCl (Fig. 3A). Compared to the bare GCE (curve a), the MWCNT-GO modified electrodes exhibited a stronger current signal (curve b) owing to the high conductivity of MWCNT-GO. The current signal further increased after the electrodeposition of the AuNP layer (curve c), which was attributed to the excellent electrical conductivity of AuNPs and the reduction of GO. The current signal decreased after the incubation of Ab_1 (curve d). The blocking of BSA caused additional current signal decreased (curve e). A further decrease in signal response was observed after the incubation of CA 125 (curve f), and again after conjunction of the immunoprobe (Ab_2-Fe^{3+}-PDA) (curve g).

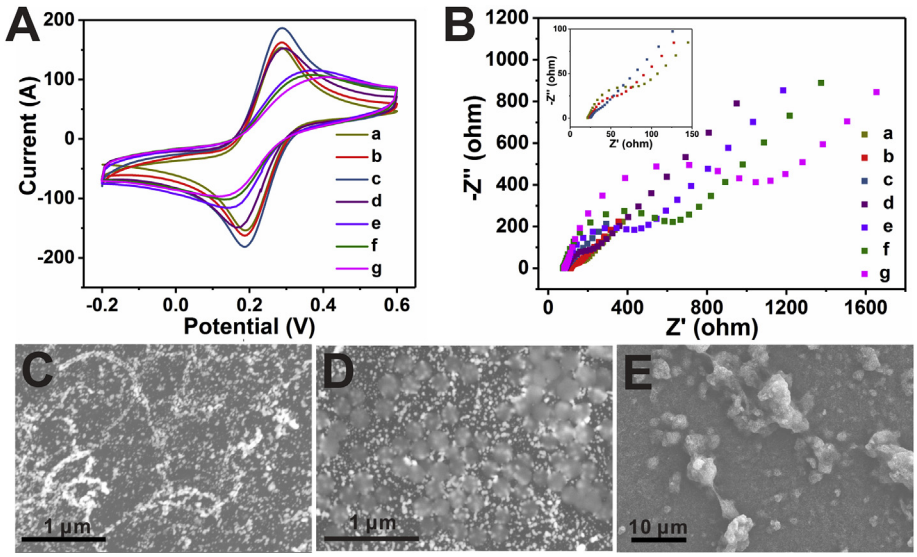

Fig. 3. CV (A) and EIS responses (B) of the different modified electrodes in 5 mM $[Fe(CN)_6]^{3-/4-}$ with 0.1 M KCl: GCE (a), MWCNT-GO/GCE (b), Au/MWCNT-GO/GCE (c), Ab_1/Au/MWCNT-GO/GCE (d), BSA/Ab_1/Au/MWCNT-GO/GCE (e), CA 125/BSA/Ab_1/Au/MWCNT-GO/GCE (f), Fe^{3+}-PDA/CA 125/BSA/Ab_1/Au/MWCNT-GO/GCE (g). SEM micrographs of Au/MWCNT-GO/GCE (C), after the assemble of Fe^{3+}-PDA (D) and after the growth of PB (E).

The sensing interface properties of the proposed immunosensor were then investigated by electrochemical impedance spectroscopy (EIS) in 5 mM $[Fe(CN)_6]^{3-/4-}$ solution containing 0.1 M KCl (Fig. 3B). In EIS detection, charge-transfer resistance (Rct) is the main indicator and corresponds to the diameter of the semicircle in Nyquist plots. The MWCNT-GO modified electrodes (curve b) displayed a smaller semicircle compared with that of the bare GCE (curve a). The semicircle decreased after the modification of Au NP layer (curve c), then increased after the incubation of Ab_1 (curve d) and blocking of BSA (curve e). The semicircle further enlarged after the incubation of CA 125 (curve f) and the conjunction of immunoprobes (Ab_2-Fe^{3+}-PDA) (curve g). These results coincide with the measurements of CV, suggesting successful modification of the immunosensor.

The construction of the immunosensor was also characterized by SEM. After the electrodeposition of the AuNP layer, AuNPs were well distributed on the MWCNT-GO/GCE (Fig. 3C). After conjunction of the immunoprobes, Ab_2-Fe^{3+}-PDA nanocomposites were scattered on Au/MWCNT-GO/GCE (Fig. 3D). Following the treatment with the PB precursor solution, PB particles were observed on the electrode surface. No Ab_2-Fe^{3+}-PDA nanocomposites were found on the electrode surface, demonstrating that the as-formed sandwich-type structure was destroyed. Fe^{3+}-PDA was decomposed by hydrochloric acid in PB precursor solution (Cheng et al., 2013). For further illustration, we reacted Fe^{3+}-PDA with the PB precursor solution in tubes and analyzed the product with TEM, which revealed only the presence of PB NPs (Fig. S1).

3.4. Optimization of experimental conditions

The concentration of HCl in PB precursor solution and the time for PB growth were crucial to the analytical performance since high concentrations of HCl and long term growth of PB may cause strong background signal. The percent signal change (signal % = $(I–I_0)/I_0 \times 100\%$. I and I_0 represent SWV peak current in 0.1 M PBS with 1 U mL^{-1} CA 125 and blank grew up in HCl concentration range of 0.0125–0.1 mM and weakened at higher concentration (Fig. S2A). High concentration of HCl caused large background signal, leading to the decrease of the percent signal change. Therefore, 0.1 mM was selected as the optimal concentration of HCl for PB growth. The percent signal change was raised with the increase of PB growth time and reached a maximum at 40 min (Fig. S2B). With the succession of PB growth, the background signal increased obviously, resulting in a decline of the percent signal change. Thereby, the optimum time for PB growth was determined as 40 min.

The volume of MWCNT-GO was found to prominently influence the conductivity of the electrochemical sensing platform. Thus, the volume of MWCNT-GO was optimized by measuring CV responses in 5 mM $[Fe(CN)_6]^{3-/4-}$ solution containing 0.1 M KCl. The current signal increased when the volume of MWCNT-GO ranged from 2.0 to 5.0 μL and remained unchanged at higher volumes (Fig. S3A). Therefore, 5.0 μL was determined as the optimum volume of MWCNT-GO. Cycles of electrodeposition of Au NP layer was also optimized (Fig. S3B) by measuring CV responses in 5 mM $[Fe(CN)_6]^{3-/4-}$ solution containing 0.1 M KCl. The current signal increased in potential cycles 3 to 6. The improvement of electrochemical activity was attributed to the modification of AuNP layer and the reduction of MWCNT-GO (Zhang et al., 2015). The current signal was reduced with the progression of cycling. Thus, the optimal cycle of electrodeposition was chosen as 6 cycles.

The immunoprobes (Ab_2-Fe^{3+}-PDA) was electrochemical inactive and Fe^{3+} in immunoprobes can reacted with PB precursor solution (a mixed solution of 0.1 M KCl, 0.1M HCl and 1 mM $K_3Fe(CN)_6$) to generate electroactive PB nanoparticles to produce electrochemical signal. Therefore, binding amount of immunoprobes affected the final electrochemical signal. The conjunction of immunoprobes takes some time to implement. The purpose of optimizing the incubation time is to achieve the full adsorption of immunoprobes thus to obtain the maximized electrochemical signal. The incubation time was studied from 20 to 60 min. The current signal (SWV response in 0.1 M PBS) increased sustainably and reached the maximum at 50 min then remained unchanged with further incubation (Fig. S4A). Hence, the optimum incubation time of immunoprobe was determined as 50 min. The electrochemical signal was affected by the pH of the detection solution significantly. To obtain the maximum current signal, the pH of the detection solution was optimized. The signal response (SWV response in 0.1 M PBS) increased with increasing pH value and a maximum signal response was observed at pH 7.0, then the signal response decreased at higher pH values (Fig. S4B). Therefore, the optimal pH value for electrochemical detection was 7.0. The optimal concentration of H_2O_2 was investigated to realize signal amplification. The SWV response increased with the increase of H_2O_2 levels from 0.25 to 1.0 mM and decreased with further addition of H_2O_2 (Fig. S4C). This was because that H_2O_2 in high concentration was adverse to electron transfer. Therefore, 1.0 mM was selected as the optimal concentration of H_2O_2.

3.5. Electroactivity conversion and catalytic amplification

Electroactivity conversion of the prepared sensing interface was researched by SWV. As displayed in Fig. 4A, no electrochemical signal

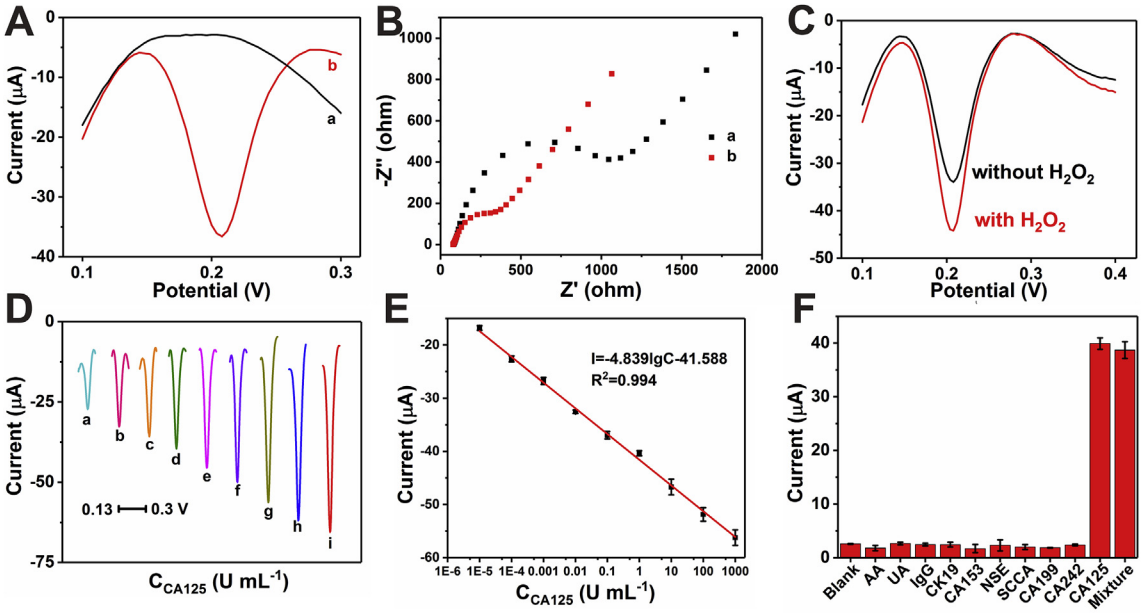

Fig. 4. SWV (A) and EIS response (B) before (a) and after (b) the growth of PB. SWV response of 1 U mL^{-1} CA125 with and without 1 mM H_2O_2 (C). SWV response toward different levels of CA 125 standards (D) and calibration curve (E). The specificity of the immunosensor. The mixture solution including AA (10 mM), UA (10 mM), IgG (100 ng mL^{-1}), CK19 (100 ng mL^{-1}), CA 153 (100 U mL^{-1}), NSE (100 ng mL^{-1}), SCCA (100 ng mL^{-1}), CA 242 (100 U mL^{-1}), CA 199 (100 U mL^{-1}), CA 125 (1 U mL^{-1}) (F).

was observed after conjunction of the immunoprobe (Ab_2-Fe^{3+}-PDA) (curve a). After the treatment with PB precursor solution, the sensing interface presented a strong current signal at 0.2 V due to the growth of PB nanoparticles (curve b).

EIS was performed to characterize the conversion of interfacial conductivity in 5 mM $[Fe(CN)_6]^{3-/4-}$ solution containing 0.1 M KCl. After the growth of PB nanoparticles (curve b), the interface impedance decreased significantly in comparison with the signal of the Ab_2-Fe^{3+}-PDA modified electrode (Fig. 4B, curve a). The as-formed sandwich-type structure was destroyed due to the decomposition of self-sacrificial Fe^{3+}-PDA caused by HCl in the PB precursor solution, leading to a prominent decrease of the interface impedance.

The sensing interface exhibited high electrocatalytic activity due to the growth of PB nanoparticles. To evaluate the catalytic amplification, 1 U mL^{-1} CA 125 was assayed by the prepared immunosensor with 1 mM H_2O_2 (curve b) and without H_2O_2 (curve a), as shown in Fig. 4C. The signal response was significantly elevated due to the catalytic amplification of PB.

3.6. Assay performance of CA 125

A series of CA 125 standard solutions with different concentrations were detected using the electrochemical immunosensor under the optimized experimental parameters. The SWV response increased with the increase of CA 125 levels from 0.00001 to 1000 U mL^{-1} (Fig. 4D), demonstrating a good linear relationship between the SWV signal and logarithm of CA 125 level (Fig. 4E). The regression equation was fitted to I = −4.839lgC-41.588, where the R^2 was 0.994, and the detection limit was 0.25×10^{-6} U mL^{-1}. Compared with other works in electrochemical sensing of CA 125, the proposed immunosensor exhibited a wider detection range, lower detection limit, and higher sensitivity (Table 1).

3.7. Specificity, reproducibility and stability of the immunosensor

In order to verify the specificity of the immunosensor, interfering substances (including ascorbic acid (AA), uric acid (UA), human immunoglobulin G (IgG), cytokeratin 19 antigen (CK19), carbohydrate antigen 153 (CA 153), neuron specific enolase (NSE), and squamous Cell Carcinoma Antigen (SCCA), carbohydrate antigen 242 (CA 242), carbohydrate antigen 199 (CA 199)) were tested using the prepared electrochemical immunosensor. The current signal toward the disturbances was proximate to that of blank. A mixture solution of these disturbances and CA 125 was also assayed and showed no significant change in comparison with CA 125 (Fig. 4F). These results revealed satisfactory specificity of the immunosensor. To evaluate reproducibility, four modified sensing interfaces were utilized to assay 1 U mL^{-1} CA 125. The difference in SWV responses of the four electrodes was negligible, and the relative standard deviation (RSD) was less than 10%, confirming excellent reproducibility. The stability of the immunosensor was also examined. The assembled immunosensor was stored at 4 °C for four weeks and tested once a week. The parallel assay results exhibited high reproducibility with an acceptable RSD below 6%.

3.8. Clinical analysis

To verify the feasibility of the electrochemical immunosensor in clinical samples, five human serum samples were tested and compared with a chemiluminescence immunoassay analyzer (CMIA) (Table S1) (Wesseling et al., 2003). The relative error ranged from −5.83% to 5.38%, illustrating prospective potential of the immunosensor in clinical application.

4. Conclusion

In summary, a sensitivity amplification strategy based on self-sacrificial label assisted electroactivity conversion of a sensing interface was developed for the sensitive determination of CA 125. As redox mediators and catalysts, PB NPs were generated in the final assembly step in order to prevent signal leaking and decreases of catalytic activity caused by layers of decoration. In addition, the large hindrance effect of immunoprobes can be eliminated through the decomposition of Fe^{3+}-PDA. This approach provided prominent enhancement of sensitivity and ultralow detection limit of 0.25×10^{-6} U mL^{-1}. If the background signal could be further decreased using more anti-fouling sensing interface, the analytical performance can be remarkably improved. We

Table 1
Comparison of the present biosensor and some previous biosensors for the detection of CA 125.

Amplification method	Linear range (U mL^{-1})	Detection limit (U mL^{-1})	Reference
Organic polymers protected prussian blue nanoparticles	2.0–100	0.71	Chen et al. (2008)
MPA/AuNP@SiO_2/QD	0–0.1	0.0016	Johari-Ahar et al. (2015)
Thionine and gold nanoparticles	10–30	1.8	Tang et al. (2006)
Polyaniline-polythionine hydrogel	0.0001–1000	0.00125	Zhao and Ma (2018)
Self-sacrificial label assisted electroactivity conversion	0.00001–1000	0.00000025	This work

expect that the proposed self-sacrificial label-assisted electroactivity conversion will advance sensitivity amplification strategies in various electrochemical immunoassays.

CRediT authorship contribution statement

Shuang Yin: Investigation, Writing - original draft. **Zhanfang Ma:** Funding acquisition, Project administration, Supervision.

Acknowledgments

This research was financed by grants from the National Natural Science Foundation of China (21673143), Natural Science Foundation of Beijing Municipality (2172016), and Capacity Building for Sci-Tech Innovation-Fundamental Scientific Research Funds (19530050179).

Appendix A. Supplementary data

Supplementary data to this article can be found online at https://doi.org/10.1016/j.bios.2019.111355.

Declaration of interest statement

The authors declare no conflict of interest.

Conflict of interest

We have no conflicts of interest to declare.

References

Atkinson, A.J., Colburn, W.A., Degruttola, V.G., Demets, D.L., Downing, G.J., 2001. Clin. Pharmacol. Ther. 69, 89–95.
Cai, G.N., Yu, Z.Z., Ren, R.R., Tang, D.P., 2018. ACS Sens. 3, 632–639.
Chao, Z., Ren, L., Wang, X., Liu, T., 2010. J. Phys. Chem. C 114, 11435–11440.
Chen, H., Jiang, J.H., Huang, Y., Deng, T., Li, J.S., Shen, G.L., Yu, R.Q., 2006. Sensor. Actuator. B Chem. 117, 211–218.
Chen, S.H., Yuan, R., Chai, Y.Q., Yang, X., Min, L.G., Na, L., 2008. Sens. Actuators, B 135, 236–244.
Cheng, F.F., Zhang, J.J., Xu, F., Hu, L.H., Abdel-Halim, E.S., Zhu, J.J., 2013. Int. J. Pharm. 9, 1155–1163.
Guo, H.L., Wang, X.F., Qian, Q.Y., 2009. ACS Nano 3, 2653–2659.
Han, E., Ding, L., Jin, S., Ju, H.X., 2011. Biosens. Bioelectron. 26, 2500–2505.
Han, Q., Wang, R.Y., Xing, B., Zhang, T., Khan, M.S., Wu, D., Wei, Q., 2017. Biosens. Bioelectron. 99, 493–499.
Hou, L., Tang, Y., Xu, M.D., Gao, Z.Q., Tang, D.P., 2014. Anal. Chem. 86, 8352–8358.
Hua, X., Qin, W., Chai, Y.Q., Yuan, Y.L., Yuan, R., 2016. Biosens. Bioelectron. 86, 630–635.
Johari-Ahar, M., Rashidi, M.R., Barar, J., Aghaie, M., Mohammadnejad, D., Ramazani, A., Karami, P., Coukos, G., Omidi, Y., 2015. Nanoscale 7, 3768–3779.
Li, J.X., Liu, F., Zhu, Z., Liu, D., Chen, X.F., Song, Y.L., Zhou, L.J., Yang, C.Y., 2018. ACS Appl. Mater. Interfaces 10, 13390–13396.
Luo, X., Davis, J.J., 2013. Chem. Soc. Rev. 42, 5944–5962.
Sawyers, C.L., 2008. Nature 452, 548–552.
Shen, W.J., Zhuo, Y., Chai, Y.Q., Yang, Z.H., Han, J., Yuan, R., 2015. ACS Appl. Mater. Interfaces 7, 4127–4134.
Tang, D.P., Yuan, R., Chai, Y.Q., 2006. Anal. Chim. Acta 564, 158–165.
Tang, D.P., Su, B.L., Tang, J., Ren, J.J., Chen, G.N., 2010. Anal. Chem. 82, 1527–1534.
Tang, L.H., Liu, Y., Ali, M.M., 2012. Anal. Chem. 84, 4711–4717.
Tang, Z.X., Fu, Y.Y., Ma, Z.F., 2017. Biosens. Bioelectron. 91, 299–305.
Wang, Z.F., Liu, N., Ma, Z.F., 2014. Biosens. Bioelectron. 53, 324–329.
Wang, Z.F., Liu, N., Feng, F., Ma, Z.F., 2015. Biosens. Bioelectron. 70, 98–105.
Wang, L.Y., Shan, J., Feng, F., Ma, Z.F., 2016. Anal. Chim. Acta 911, 108–113.
Wei, Y.C., Li, X.J., Sun, X., Ma, H.M., Zhang, Y., Wei, Q., 2017. Biosens. Bioelectron. 94, 141–147.
Wesseling, S., Stephan, C., Semjonow, A., Lein, M., Brux, B., Sinha, P., Clin. Chem. 49, 887-894.
Wilson, M.S., 2005. Anal. Chem. 77, 1496–1502.
Xu, T., Liu, N., Yuan, J., Ma, Z.F., 2015. Biosens. Bioelectron. 70, 161–166.
Yang, F., Yang, Z.H., Zhuo, Y., Chai, Y.Q., Yuan, R., 2015a. Biosens. Bioelectron. 66, 356–362.
Yang, Z.H., Zhuo, Y., Yuan, R., Chai, Y.Q., 2015b. Biosens. Bioelectron. 69, 321–327.
Yin, S., Zhao, L.H., Ma, Z.F., 2017. Anal. Bioanal. Chem. 410, 1279–1286.
Zhang, Y., Ji, Y., Wang, Z.Y., Liu, S., Zhang, T., 2015. RSC Adv. 5, 106307–106314.
Zhang, X.N., Shen, J.D., Ma, H.L., Jiang, Y.X., 2016. Biosens. Bioelectron. 80, 666–673.
Zhang, D.S., Li, W.X., Ma, Z.F., 2018. Biosens. Bioelectron. 109, 171–176.
Zhao, L.H., Ma, Z.F., 2018. Anal. Chim. Acta 997, 60–66.
Zhao, L.H., Han, H.L., Ma, Z.F., 2018. Biosens. Bioelectron. 101, 304–310.
Zhao, L.H., Yin, S., Ma, Z.F., 2019. ACS Sens. 4, 450–455.
Zheng, Y., Ma, Z.F., 2018. Biosens. Bioelectron. 108, 46–52.
Zhou, J., Han, T.Q., Ma, H.M., Yan, T., Pang, X.H., Li, Y.Y., Wei, Q., 2015. Anal. Chim. Acta 889, 82–89.